Photoisomerization transition state manipulation by entangled two-photon absorption

Bing Gu[a,b,1], Daniel Keefer[a,b,1], Flavia Aleotti[c], Artur Nenov[c], Marco Garavelli[c], and Shaul Mukamel[a,b,2]

[a]Department of Chemistry, University of California, Irvine, CA 92697; [b]Department of Physics & Astronomy, University of California, Irvine, CA 92697; and [c]Dipartimento di Chimica Industriale "Toso Montanari," Università degli studi di Bologna, 40136 Bologna, Italy

We demonstrate how two-photon excitation with quantum light can influence elementary photochemical events. The azobenzene *trans → cis* isomerization following entangled two-photon excitation is simulated using quantum nuclear wave packet dynamics. Photon entanglement modulates the nuclear wave packets by coherently controlling the transition pathways. The photochemical transition state during passage of the reactive conical intersection in azobenzene photoisomerization is strongly affected with a noticeable alteration of the product yield. Quantum entanglement thus provides a novel control knob for photochemical reactions. The distribution of the vibronic coherences during the conical intersection passage strongly depends on the shape of the initial wave packet created upon quantum light excitation. X-ray signals that can experimentally monitor this coherence are simulated.

entangled photons | two-photon absorption | photoisomerization | azobenzene | wave packets

Quantum spectroscopy, which makes use of the quantum nature of light to extract new information about matter, is made possible by recent developments in quantum optics (1). Conventional classical spectroscopy uses laser light to detect the optical properties of molecules and materials by varying laser frequencies or interpulse time delays (2). By exploiting the squeezing and entanglement of quantum states of light as novel control knobs, quantum light opens up new avenues for spectroscopy. Quantum spectroscopy has been demonstrated, both theoretically and experimentally, to be a powerful tool for revealing novel information about complex molecules and enhancing the signal-to-noise ratio and resolution beyond what is possible with classical light (3, 4). The incoming photon statistics can be employed to improve the selectivity of optical response functions of matter (5), and quantum two-photon interferometers such as the Hong-Ou-Mandel and Franson's (6) can be used to design novel signals which have no classical analogs (7–9).

The simplest quantum light spectroscopic techniques, entangled two-photon absorption (ETPA), has attracted broad attention (9–24). In this technique, the molecule is promoted from the ground state to an excited state by simultaneous absorption of two entangled degenerate or nondegenerate photons. Here we exploit ETPA to trigger the azobenzene photoisomerization reaction. This is a textbook photochemical reaction connecting the *cis* and *trans* isomers through a conical intersection (CoIn). Azobenzene-based photoswitches have found broad application as functional units in biology (25) and material science (26). Their isomerization can be switched selectively in both directions with high quantum yield using different wavelengths (27–29). The activity of ion channels, lipids, neurons, pharmaceutical drugs, charge carriers, and protein folding can be regulated by chemically incorporating azobenzenes at the active sites (25, 26, 30). For these reasons, the ultrafast dynamics of azobenzene upon photoexcitation has been extensively studied (supplement in ref. 29). The isomerization occurs in the S_1 electronic potential energy surface (PES), which has a very weak oscillator strength in the one-photon transition. The *trans → cis* isomerization can be initiated by ultraviolet (UV) excitation to the optically bright $\pi\pi^*$ S_2 state (28, 29, 31), which then decays in ~ 100 fs to the lower

$n\pi^*$ S_1 state (29, 31). Isomerization then occurs in S_1 through a reactive CoIn with S_0 between the *trans* and *cis* structures (32). However, this has a lower quantum yield. A second possibility is direct excitation to the reactive S_1 state by two-photon absorption as demonstrated repeatedly in experiments (33–35), where the isomerization then occurs with almost double the quantum yield, thus violating Kasha's rule (29, 31, 36). Near-infrared light, in contrast to UV/visible wavelengths used in the one-photon processes, can better penetrate tissues without photodamage (37), thus enabling selective switching in biological environments (25, 30). Azobenzene multiphoton excitation further offers three-dimensional submicron spatial resolution (38).

Here we directly excite azobenzene to the reactive S_1 electronic state using an entangled photon pair and investigate the ability of the quantum light parameters to manipulate the resulting photodynamics. By using nonadiabatic wave packet dynamics simulations, we demonstrate that photon entanglement provides a powerful tool to study the complex interplay of reactive and nonreactive CoIns that determines the quantum yield of the reaction. ETPA differs from the classical counterpart (classical two-photon absorption [CTPA]) in many ways. At low photon fluxes, it scales linearly rather than quadratically with the pump intensity (23, 39). This is because the entangled photon pairs generated by, e.g., spontaneous parametric downconversion (SPDC) (40, 41) are born at the same time and interact with molecules simultaneously. Furthermore, twin photons generated by a

Significance

Entangled two-photon absorption has attracted considerable interest due to its potential applications for low–photon flux spectroscopy and microscopy. The entanglement parameters in the twin-photon state can be exploited to control two-photon excitation processes. Here we demonstrate that photon entanglement provides a powerful novel control knob for the nuclear wave packets in an optically dark electronic state. We show that the transition states in the trans–cis photoisomerization of azobenzene, initiated by an entangled two-photon absorption process, can be manipulated significantly by entangled light. These effects can be monitored experimentally by coherent stimulated X-ray Raman signals which reveal electronic coherences during the passage through conical intersections.

narrowband pump exhibit a strong energy anticorrelation; that is, detection of one photon reveals the frequency of its twin within a small uncertainty determined by the pump bandwidth. This energy–time entanglement may be used to manipulate the quantum interference among transition pathways. Entangled photon pairs have been shown to induce classically forbidden collective excitations (42) and to probe classically dark bipolariton states (19). Since the ETPA signal depends on the incoming entangled photon pair (biphoton) statistics, the two-photon excitation process can be coherently controlled by tuning the biphoton state.

The ETPA Signal

In the setup schematically shown in Fig. 1, a pump pulse creates an entangled photon pair, known as signal and idler, through interaction with a second-order nonlinear crystal. The photon pair then brings the azobenzene molecule to the S_1 excited state by two-photon absorption, launching the photoisomerization process.

The ETPA signal is commonly detected by fluorescence from the excited states. However, for molecules undergoing CoIns, nonradiative processes dominate the excited state dynamics, thus reducing the fluorescence yield. We thus define the signal by the isomerization rate $S = \lim_{t \to \infty} \frac{dP(t)}{dt}$, where $P(t) = \langle \Psi(t)|\mathcal{P}|\Psi(t)\rangle$ is the population of product defined by the projection operator $\mathcal{P}$ and $|\Psi\rangle$ refers to the joint photon–electron–nuclear state. For the *trans → cis* isomerization, the projection operator can be formally defined as the torsion angle $q_1 \equiv$ C1–N1–N2–C2 (CNNC, see Fig. 1) in the range $(-\pi/2, \pi/2)$, i.e., $\mathcal{P} = \int d\mathbf{q}\,\theta(|q_1| < \pi/2)\,|\mathbf{q}\rangle\langle\mathbf{q}|$ where $\mathbf{q}$ denotes the internal nuclear coordinates and $\theta = 1$ if $|q_1| < \pi/2$ and 0 otherwise. The ETPA signal can then be calculated using time-dependent perturbation theory (43) (*SI Appendix*, section S1), which gives

$$
P(t) = \sum_{\mathbf{p}} \int_{t_0}^{t} dt_2 \int_{t_0}^{t_2} dt_1 \int_{t_0}^{t} dt_2' \int_{t_0}^{t_2'} dt_1'
$$

$$
\left\langle \psi_0(\mathbf{q})\chi_0 \left| \mu_{p_1'}(t_1')\mu_{p_2'}(t_2')\mathcal{P}(t)\mu_{p_2}(t_2)\mu_{p_1}(t_1) \right| \psi_0(\mathbf{q})\chi_0 \right\rangle
$$

$$
\times\, G_{\mathbf{p}}^{(2)}(t_1', t_2', t_2, t_1),
$$

[1]

where $G_{\mathbf{p}}^{(2)}(t_1', t_2', t_2, t_1) \equiv \langle E_{p_1'}^{(-)}(t_1')E_{p_2'}^{(-)}(t_2')E_{p_2}^{(+)}(t_2)E_{p_1}^{(+)}(t_1)\rangle$ is the field correlation function and $E_{p_i}^{(+)}(t)$ ($E_{p_i}^{(-)}(t)$) is the positive (negative) frequency component of the electric field operator of the p_i beam (44), and $\mu_{p_i}(t) = U_{\mathrm{M}}^{\dagger}(t)\boldsymbol{\mu} \cdot \mathbf{e}_{p_i} U_{\mathrm{M}}(t)$ denotes the dipole operator $\boldsymbol{\mu}$ projected on the polarization $\mathbf{e}_{p_i}$ in the interaction picture with $U_{\mathrm{M}}(t)$ being the interaction-free molecular propagator. Eq. 1 can be represented by the time loop diagram shown in Fig. 2, where the photon indices $\mathbf{p} = (p_1', p_2', p_2, p_1)$, $p_i = \{s, i\}$ are ordered along the time loop clockwise. The initial molecular state $|\psi_0(\mathbf{q})\chi_0\rangle$, where $|\psi_\alpha(\mathbf{q})\rangle$ denotes the αth adiabatic electronic state, describes the ground vibrational state $|\chi_0\rangle$ in the ground electronic
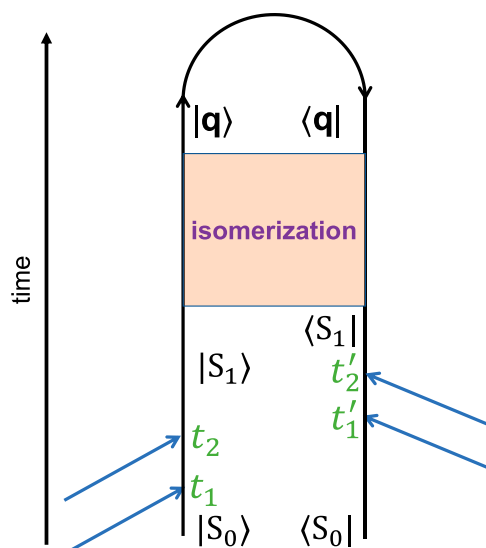

Fig. 1. Azobenzene *trans → cis* isomerization initiated by entangled two-photon absorption. The combined energy of the two photons matches the S_0/S_1 transition at the *trans* geometry. The first reactive nuclear coordinate q_1 is the C1–N1–N2–C2 dihedral angle, and the second coordinate q_2 is the symmetric bending of the C1–N1–N2 and N1–N2–C2 angles.

Fig. 2. Time loop diagram for Eq. 1 representing the ETPA followed by a chemical reaction.

PES. The field correlation function can be used to control the two-photon excitation process by tuning the incoming biphoton statistics. For a pure two-photon state, $G^{(2)}$ can be factorized by $G_{\mathbf{p}}^{(2)}(t_1', t_2', t_2, t_1) = A_{p_2'p_1'}^{*}(t_2', t_1')A_{p_2p_1}(t_2, t_1)$, where $A_{p_2p_1}(t_2, t_1) \equiv \langle 0|E_{p_2}^{(+)}(t_2)E_{p_1}^{(+)}(t_1)|\Phi_0\rangle$ is the two-photon detection amplitude (*SI Appendix*, section S2). In this case, Eq. 1 reduces to (set the vibronic ground state energy to zero)

$$
P(t) = \int d\mathbf{q}\,\theta(q_1 < \pi/2) \left| \sum_{p_2 \neq p_1} \int_{t_0}^{t} dt_2 \int_{t_0}^{t_2} dt_1 \right.
$$

$$
\left. \langle \mathbf{q} | U_{\mathrm{M}}(t - t_2)\mu_{p_2} U_{\mathrm{M}}(t_2 - t_1)\mu_{p_1} | \psi_0(\mathbf{q}), \chi_0 \rangle A_{p_2p_1}(t_2, t_1) \right|^2.
$$

[2]

The condition $p_1 \neq p_2$ ensures that the molecules absorb photons from different beams. Eq. 2 is our final result that will be computed numerically. The detection amplitude is determined by the entangled light employed, whereas the molecular propagator in Eq. 2 is computed by nuclear wave packet dynamics (*SI Appendix*, section S3). For CTPA, the two-photon transition amplitude is replaced by the electric field $\mathcal{E}_{p_2}(t_2)\mathcal{E}_{p_1}(t_1)$, and pathways with $p_1 = p_2$ must be included as the molecule can absorb two photons from a single classical pulse.

The *trans → cis* Isomerization of Azobenzene

The process can be initiated by optical excitation either to the dipole-allowed $\pi\pi^*$ S_2 or the dipole-forbidden $n\pi^*$ S_1 state (29, 31). Compared to S_2 excitation, direct population of S_1 doubles the photoisomerization yield, in violation of Kasha's rule (36). This has puzzled researchers for many years. High-level complete active space second-order perturbation theory (CASPT2) PESs of the relevant electronic states along the isomerization path were recently reported (32). The relevant nuclear space is spanned by three degrees of freedom, with the first being the CNNC dihedral angle (Fig. 1) that connects the *trans* with the *cis* minimum at 180° and 5°, respectively. The second and third degrees of freedom are the C1–N1–N2 (CNN) and N1–N2–C2 bending angles (Fig. 1).

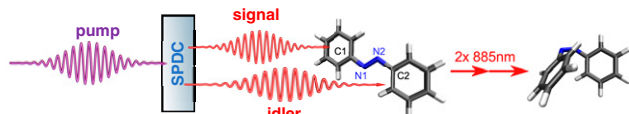Earlier, we had employed an effective two-dimensional Hamiltonian for the other *cis* → *trans* direction of the isomerization (45). Fixing one of the two CNN bending angles was required to achieve symmetry breaking and reach the minimum energy reactive CoIn. The PESs and semiclassical dynamics in ref. 32 reveal that the excited *trans* molecule evolves first along symmetric bending, and energy is then transferred to the CNNC torsion. Thus, to perform nuclear wave packet simulations describing the *trans* → *cis* isomerization, we use an effective Hamiltonian with the reactive CNNC dihedral and the symmetric CNN bending coordinate. The S_1 and S_0 PESs are depicted in Fig. 3, along with the nonadiabatic couplings (NACs) responsible for the non–Born–Oppenheimer effects and wave packet relaxation during the dynamics. The NACs were calculated at the same level of theory as the PESs by atomic displacement along the internal coordinates. As is apparent from Fig. 3, the *trans* → *cis* isomerization is blocked in the ground state by a 2-eV barrier. In S_1, the main gradient from the Franck–Condon (FC) point points in the symmetric bending direction, keeping the in-plane symmetry. A shallow local minimum with 2.1 eV energy exists at CNNC = 180° and CNN = 126°. From here, along the CNNC torsion, a small 0.2-eV barrier exists that is, however, lower than the FC in S_1 lying at 2.5 eV. Isomerization in S_1 is thus possible at the path from FC to the reactive CoIn seam that stretches from CNNC = 90° to 105° and from CNN = 115° to 155°, with the strongest coupling region around CNNC = 100° and CNN = 143°.

The NACs in Fig. 3 are responsible for population transfer of the nuclear wave packet between the adiabatic states. Their calculation involves terms of type $\langle \psi_0 | \frac{\partial}{\partial q_i} | \psi_1 \rangle$, i.e., overlap integrals of two adiabatic electronic wave functions ψ, where one of them is displaced along the internal nuclear coordinate q_i, thus mixing electronic and nuclear degrees of freedom. The nuclear coordinates q_1 = CNNC and q_2 = CNN yield two NACs displayed in Fig. 3. The reactive CoIn seam is located between the *cis* and *trans* geometries and thus allows the molecule to relax back to S_0 on the isomerization pathway. Both q_1 and q_2 induce significant NAC.

A nonreactive CoIn seam at larger symmetric bending angles (around 150°) is well established. We have calculated the NAC scanning symmetric CNN bending angles from 100° to 180° at fixed CNNC = 180° in *SI Appendix*, section S4. This NAC is highly peaked at CNN = 150°, while it is almost vanishing along CNNC. We observe very weak mixing of the S_0 and S_1 CASPT2 wave function, suggesting a real crossing of the two states. The same behavior is observed for identical scans at different CNNC dihedral angles when S_0 and S_1 come close in energy. We thus replicated the calculated NAC profile for the CNNC = 180° scan along the CNNC direction at the minimal energy difference along CNN, thus creating the nonreactive CoIn seam depicted in Fig. 3, which is only relevant in CNN direction and vanishes for CNNC.

The two possible pathways for the nuclear wave packet launched at the FC point upon optical excitation to S_1 are marked with black (nonreactive) and magenta (reactive) in Fig. 3. The first step along the nonreactive pathway involves wave packet evolution along CNN, keeping the planar symmetry. If the wave packet reaches the nonreactive CoIn seam at CNN = 150°, it will relax to S_1 without having picked up momentum along CNNC. Step 2 is evolution back to the *trans*-S_1 minimum, and thus, no isomerization happens. If, upon excitation, the wave packet is able to pick up momentum along CNNC and thus break the planar symmetry, there is a clear path to the reactive CoIn (magenta arrows in Fig. 3). It can then relax to S_0, where the momentum gained in S_1 is preserved and further barrierless evolution to the *cis*-S_0 minimum occurs; thus, the photochemical reaction can be completed.

The Nuclear Wave Packet Created by ETPA

The signal in Eq. **1** depends on the field correlation function of the entangled photons. There are multiple ways to create entangled photon pairs such as cascaded emission and SPDC
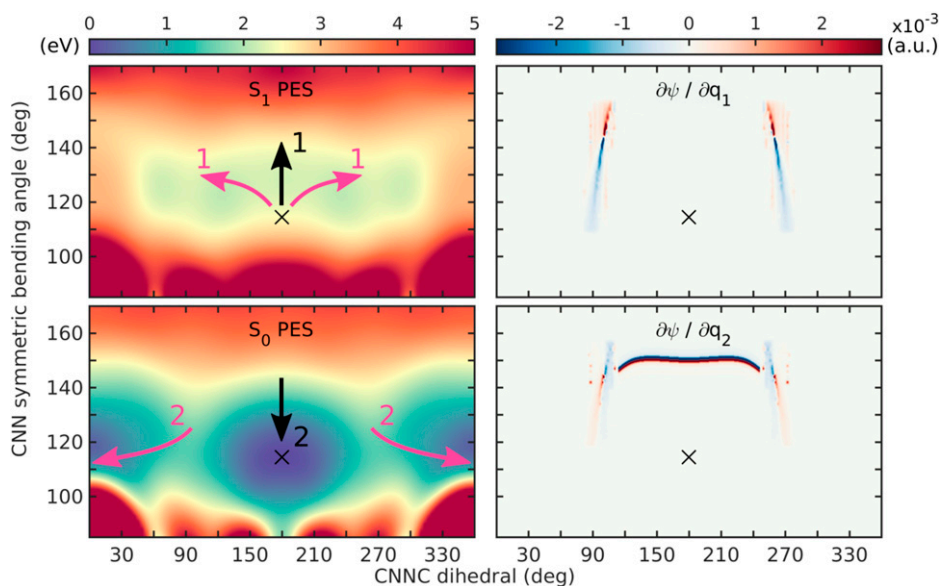
Fig. 3. (*Left*) Potential energy surface of the S_1 (*Top*) and S_0 (*Bottom*) electronic states in the two-dimensional nuclear space (q_1, torsion; q_2, symmetric bending). The *trans*-azobenzene minimum is marked with the black cross. Isomerization to *cis*-azobenzene is prevented by a 2-eV barrier in S_0 but possible in S_1. The reactive pathway is marked in magenta by 1) symmetry breaking of the molecular plane and wave packet evolution to the reactive CoIn and 2) continuing the CNNC torsional motion after relaxation to S_0, thus completing the photochemical reaction. The nonreactive pathway is marked in black with 1) keeping the planar symmetry and relaxing via the nonreactive CoIn and 2) evolving back to the *trans* minimum in S_0. (*Right*) NACs between S_0 and S_1 are calculated on the same level of theory (*SI Appendix*, section S3) while keeping track of the phase of the electronic wave function. The nonreactive seam keeps the planar molecular symmetry (CNNC = 180°) at symmetric bending values around CNN ≈ 150°. The reactive CoIn seam breaks the planar symmetry and opens the *trans* → *cis* isomerization pathway.

Gu et al.
Photoisomerization transition state manipulation by entangled
two-photon absorption

PNAS | 3 of 9
https://doi.org/10.1073/pnas.2116868118

processes, leading to two-photon states with different features. To excite *trans*-azobenzene to S_1, we employ the twin, signal and idler, photons, generated by a type II SPDC process (41, 46, 47). The entangled photon pair state is given by $|\Phi\rangle = \iint_0^\infty d\omega_s\, d\omega_i\, J(\omega_s, \omega_i) a_1^\dagger(\omega_s) a_2^\dagger(\omega_i) |0\rangle$, where $J(\omega_s, \omega_i)$ is the joint spectral amplitude (JSA) describing the signal photon with frequency ω_s and idler photon with frequency ω_i, and $a_j(\omega)$ $(a_j^\dagger(\omega))$ annihilates (creates) a j photon with frequency ω satisfying $[a_j(\omega), a_{j'}^\dagger(\omega')] = \delta_{jj'}\delta(\omega - \omega')$. We focus on the frequency anticorrelation of the entangled photons, suppressing the spatial degrees of freedom (46, 48). For a Gaussian pump pulse with bandwidth σ_p, the type II SPDC JSA is described by (43)

$$f(\Delta_s, \Delta_i) = \mathcal{N} \exp\left(-\frac{(\Delta_s + \Delta_i)^2}{4\sigma_p^2}\right)$$
$$\times \operatorname{sinc}\left(\frac{1}{2}\bar{T}(\Delta_s + \Delta_i) + \frac{1}{2}(\Delta_s - \Delta_i) T_e\right), \quad [3]$$

where $\Delta_j = \omega_j - \bar{\omega}_j$ and $\bar{\omega}_j$ is central frequency of the j photon, $T_e = \frac{1}{2}\left(\frac{L}{v_s} - \frac{L}{v_i}\right)$ is the entanglement time characterizing the difference between the arrival times of the photon pair, $\bar{T} = \frac{1}{2}\left(\frac{L}{v_s} + \frac{L}{v_i}\right) - \frac{L}{v_p}$ is the travel time difference between the biphoton and the pump inside the nonlinear crystal, and $\mathcal{N}$ is a normalization constant. The entanglement time sets an upper bound of how long the twin photons can separate in time. It fundamentally differs from the time delay between two classical pulses as separable pulses cannot violate $\sigma_{t_1-t_2}\sigma_{\omega_1+\omega_2} \geq 1$, where σ_x denotes the variance of x (49). The entangled light excitation process was simulated using the protocol detailed in ref. 43. It is given by a sum over all transition pathways each determined by the two light–matter interaction times t_2, t_1 sampled on a time grid. Each transition pathway for a fixed (t_2, t_1) is simulated by wave packet dynamics on the intermediate and final PESs. The two-photon–excited wave packet is finally obtained by numerical integration over the t_1, t_2 grid. The initial quantum light excitation process is relatively short (tens of fs) compared with the isomerization dynamics (1 ps) so that they can be separately considered.

Fig. 4 shows the nuclear wave packets in the S_1 surface excited by an entangled photon pair with different entanglement times. Clearly, the nuclear wave packets in S_1 varies with the entanglement time. The wave packet excited by entangled photons with $T_e = 6$ fs is more delocalized compared to $T_e = 1$ fs. The variation of the nuclear wave packet shape over T_e is periodic with ~ 3 fs.

To rationalize these observations, we turn to the sum-over-states expression for the transition amplitude, whose modulus squared gives the transition probability to final states (43). We expand the transition amplitude $T_{fg}(t) = \int_{t_0}^t dt_2 \int_{t_0}^{t_2} dt_1 \langle f| U_M(t - t_2)\mu_i U_M(t_2 - t_1)\mu_s |g\rangle A_{is}(t_2, t_1) + (s \leftrightarrow i)$ (cf. Eq. **2**) from the ground vibronic state $|g\rangle$ to a final vibronic state $|f\rangle$ in S_1 by summing over all intermediate eigenstates. Here $(s \leftrightarrow i)$ denotes a contribution from exchanging the s and i labels in the first term. Although obtaining all eigenstates of a molecular Hamiltonian is numerically expensive, the sum-over-states expression provides useful insights into the T_e dependence of the excited wave packet. Let $\{v\}$ denote the vibronic eigenstates in higher-lying excited state PES (e.g., S_2); the final transition amplitude is given by (43)
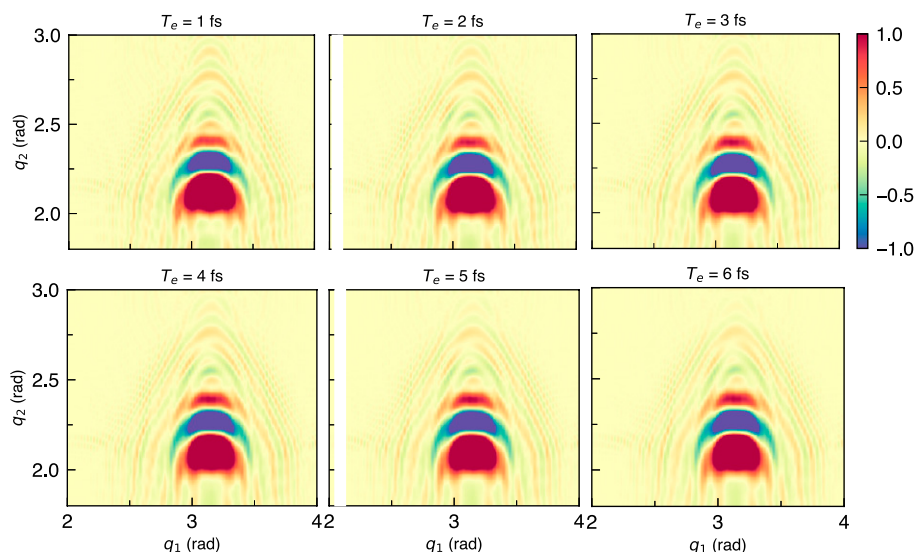
$$T_{fg} \propto \exp\left(-\frac{(\omega_{fg} - \bar{\omega}_s - \bar{\omega}_i)^2}{4\sigma_p^2}\right) \sum_v \mu_{fv}^{(i)}\mu_{vg}^{(s)} \frac{e^{i\Delta_v T_e} - 1}{i\Delta_v}$$
$$+ (s \leftrightarrow i), \quad [4]$$

where $\Delta_v = \frac{1}{2}\omega_{fg} - \omega_{vg}$ is approximately the energy difference between the S_0–S_2 gap and the incoming photon energy. For our choice, $\Delta_v \sim 1$ eV, which leads to a periodicity around $2\pi/\Delta_v \approx 3$ fs. The transition dipole moment matrix elements in Eq. **4** are between vibronic states, i.e., FC factors. The exponential factor comes from the pump spectral envelope, whereas the phase factor comes from the phase-matching condition in Eq. **3**. The two-photon excited nuclear wave packet in S_1 is a superposition of many nuclear eigenstates in the S_1 PES determined by the pump pulse bandwidth, instead of the signal/idler bandwidth. Eq. **4** reveals that the transition amplitude to each final vibronic state varies strongly on T_e due to the phase factor $e^{i\Delta_v T_e}$, which then results in a dependence of the created nuclear wave packet on the entanglement time.

To unveil the role of entanglement in the two-photon excitation process, we contrast the nuclear wave packets created by quantum light with those created by classical two-photon excitation including the chirped and nonchirped pulses. Frequency anticorrelation can also be achieved in classically correlated light (50). For example, the classically correlated light $\rho = \iint d\omega_s\, d\omega_i |f(\omega_s, \omega_i)|^2 |\omega_s\rangle\langle\omega_s| \otimes |\omega_i\rangle\langle\omega_i|$ exhibits the same joint
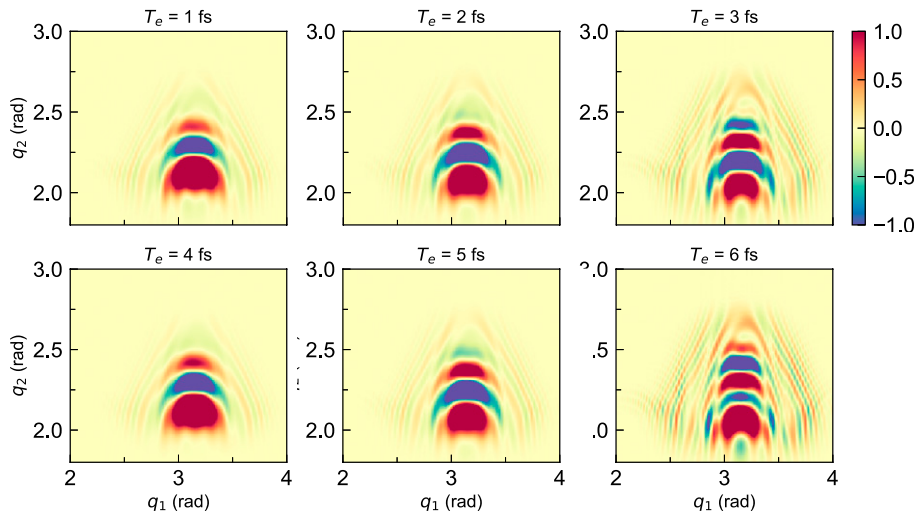
Fig. 4. Entangled two-photon excited nuclear wave packets in the S_1 surface at $t = 20$ fs varying the entanglement time T_e as indicated. The other parameters are $\bar{T} = 0$, $\sigma_p = 0.4$ eV.

Gu et al.
Photoisomerization transition state manipulation by entangled
two-photon absorption

Fig. 5. Classical two-photon excited nuclear wave packets in the S_1 surface at $t = 20$ fs with Gaussian pulses. The bandwidth is varied in correspondence to different entanglement times T_e used in Fig. 4 as indicated. The excited wave packets shows negligible dependence on the bandwidth.

spectral intensity as the entangled photon pair; nevertheless, such states cannot be used to create coherent nuclear wave packets.

Classical Gaussian Pulses. We first consider two uncorrelated classical Gaussian laser pulses with bandwidth resembling the signal and idler photons for a given JSA. The electric field of the classical pulses (for convenience, also labeled by s,i) reads

$$E_j(\omega_j) = A_j \exp\left(-\frac{(\omega_j - \bar{\omega}_j)^2}{4\sigma_j^2}\right), \qquad [5]$$

where A_j is the field amplitude. The signal/idler mode bandwidth is given by $\sigma_j^2 = \iint d\omega_s \, d\omega_i |f(\omega_s, \omega_i)|^2 \Delta_j^2$ where $j = $ s, i, which explicitly depends on the JSA. Such pulses exhibit a power spectrum resembling the quantum light, i.e., $E_j^*(\omega) E_j(\omega) \propto \langle a_j^\dagger(\omega) a_j(\omega) \rangle_q$. The electric field in the time domain reads $E_j(t) = A_j 2\sigma\sqrt{\pi} e^{-\sigma^2 t^2}$.

Fig. 5 shows that without signal-idler entanglement, variation of the incoming pulses bandwidth hardly affects the prepared nuclear wave packet. The frequency anticorrelation is thus essential for the modifications in the entangled photon pair excitation.
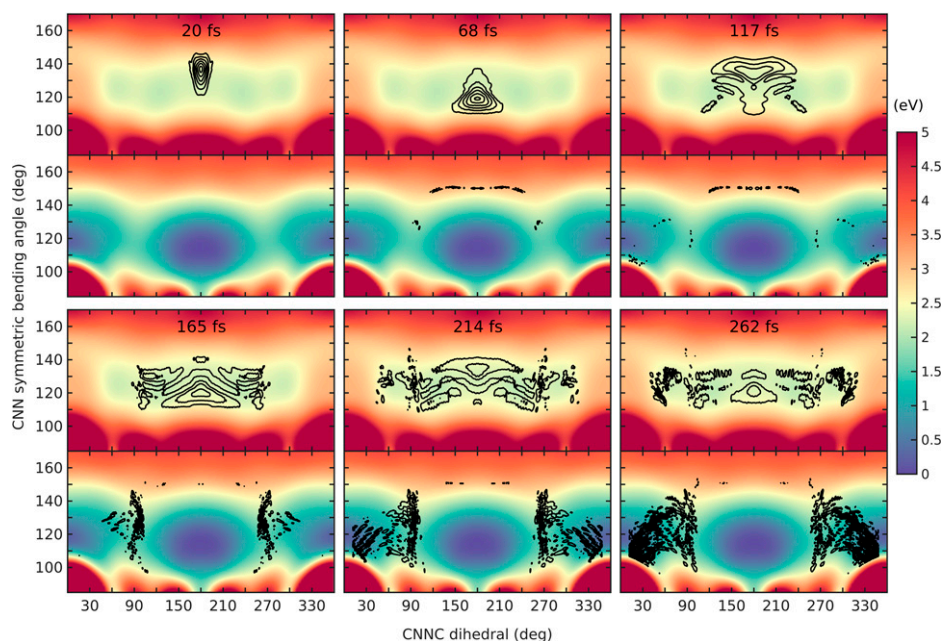
Fig. 6. Typical wave packet evolution after classical two-photon absorption. Each of the six panels contain the S_1 (top) and S_0 (bottom) potential energy surface with nuclear wavepacket snapshots at 68 fs, 117 fs, 165 fs, 214 fs, and 262 fs. The starting wave packet at 20 fs corresponds to Fig. 5 with $T_e = 1$ fs. After 68 fs, the wave packet returns back to the FC region in S_1. Very small parts have relaxed through the nonreactive pathway or reached the reactive CoIn. At 117 fs, the planar symmetry starts to substantially decrease with major parts of the wave packet starting to evolve along the CNNC torsion. The snapshots on the bottom illustrate how the wave packet predominantly follows the reactive pathway and reaches the *cis* product minimum.

Gu et al.
Photoisomerization transition state manipulation by entangled
two-photon absorption

PNAS | 5 of 9
https://doi.org/10.1073/pnas.2116868118

Classical Pulses with Long Frequency Tails. To uncover whether the control is due to the long tails in the sinc phase matching function of quantum light, we simulate with two-photon excitation with classical pulses containing similar features, i.e.,

$$E_j(\omega) = A_j \text{sinc}\left(\sigma_j\left(\omega_j - \bar{\omega}_j\right)\right). \qquad [6]$$

SI Appendix, Fig. S1 shows unnoticeable differences in the two-photon excited nuclear wave packets by varying the bandwidth, similar to the wave packets created by the Gaussian pulses despite the long tails in the spectral profile. This suggests that the single-photon resonances caused by long frequency tails are not the reason for the modulations induced by entanglement time in Fig. 4.

Linearly Chirped Gaussian Pulse. We consider the following chirped pulse:

$$\mathcal{E}_j(t) = A_j \exp\left[-\frac{1}{2}\left(t/\tau_j\right)^2\right]\exp\left[-i\left(\bar{\omega}_j t + \beta_j t^2\right)\right], \qquad [7]$$

where the phase $\beta_j t^2$ accounts for the chirping. The instantaneous angular frequency of the pulse reads $\omega_j(t) \equiv \frac{d\phi}{dt} = \bar{\omega}_j + 2\beta_j t$. We let $\beta_i = -\beta_s = \beta$ such that the sum of the instantaneous frequencies of the two pulses can be narrowly distributed, mimicking the frequency anticorrelation of entangled light.

SI Appendix, Fig. S2 shows the wave packets created by the two-photon excitation with chirped pulses with their bandwidth matching the quantum light. They do not exhibit a strong dependence on the bandwidth, which implies that the control with entangled light cannot be reproduced with chirping. While the chirped light can have a narrow distribution of the instantaneous

frequency, there is no temporal correlation between the two positively and negatively chirped pulses to ensure that the molecule interacts with the two pulses simultaneously.

Isomerization Dynamics Launched by Entangled Two-Photon Excitation

We had performed quantum dynamical propagations according to the time-dependent Schrödinger equation on the adiabatic PESs in Fig. 3. This numerical procedure is exact for the model Hamiltonian that contains two nuclear degrees of freedom. We first discuss the typical numerical propagation for the wave packet depicted on the top left in Fig. 5 upon excitation with two nonentangled near-infrared (IR) photons. Snapshots of this propagation are shown in Fig. 6 starting at 20 fs after the intensity maximum of the near-IR pulse. Within 20 fs, the wave packet starts to evolve to higher CNN values while retaining the planar symmetry in CNN; at 68 fs, it has bounced back to the FC, while very small parts have relaxed to S_0 through the nonreactive CoIn seam. When evolving to higher CNN values for the second time, the planar symmetry starts to break, and the wave packet spreads along CNNC. This is already visible at 117 fs and becomes more pronounced at 165 fs (compare Fig. 6). At 165 fs, considerable parts of the wave packet have reached the reactive CoIn seam and start to relax to S_1. As can be clearly seen from the 214 and 262 fs snapshots in Fig. 6, the planar symmetry is completely broken, and the wave packet broadly spreads along CNNC in S_1. In S_0, major parts of the wave packet have reached the *cis*-S_0 minimum, thus completing the photoisomerization. Once this minimum is reached, we absorb the nuclear wave packet with a Butterworth filter operation (51). In reality, vibrational relaxation to other modes will redistribute the kinetic energy, thus preventing major
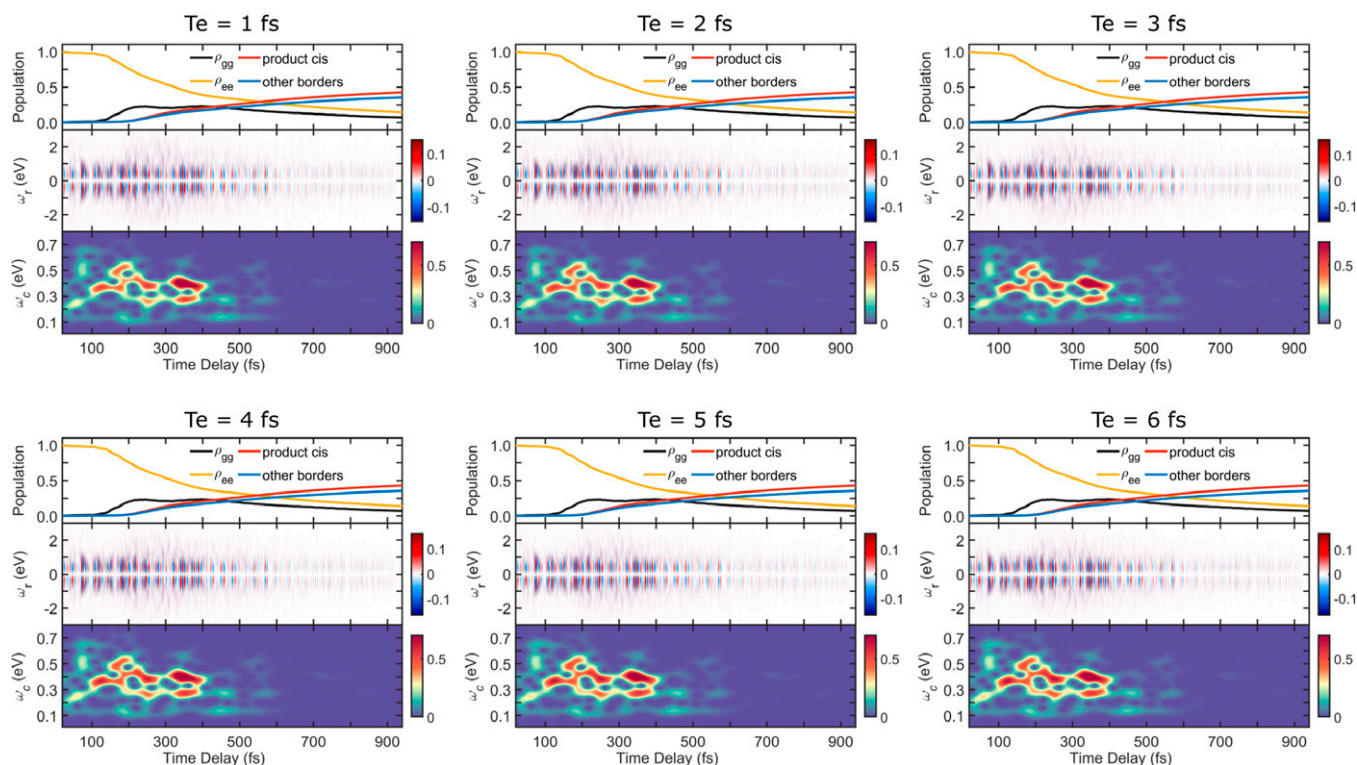
Fig. 7. Photoisomerization dynamics following two-photon excitation with classical light. Panels correspond to Fig. 5 where the starting wave packets are displayed, which are very similar. For each set of three panels, *Top* shows population dynamics with the ground and exited state populations ρ_{gg} and ρ_{ee}, the product yield as the cumulative amount of wave packet that has been absorbed in the *cis* minimum, and the cumulative amount of population that has been absorbed at the symmetric bending grid borders. *Middle* shows TRUECARS signal according to Eq. **8** being strong from the beginning, as parts of the nuclear wave packet immediately reach the CoIns and fading out with time. *Bottom* shows spectrogram of the TRUECARS signal according to Eq. **9** revealing the vibronic coherence distribution.

parts of the wave packet from continuing along the dihedral bending and crossing the 2-eV barrier in the ground state back to the *trans* minimum or even evolving back to S_1 through the CoIn. This vibrational relaxation is not captured by our two-dimensional Hamiltonian, and absorbing the wave packet in the product minimum prevents these artifacts.

This wave packet propagation explains the violation of Kasha's rule. Directly exciting S_1 provides enough energy for the wave packet to reach the nonreactive CoIn seam close to CNN = 150°, only for the small tails. The vast majority of the wave packet bounces back to the FC and subsequently breaks the planar symmetry to evolve toward the reactive pathway. Excitation to S_2 places the wave packet higher on the potential energy landscape. After a sub–100-fs relaxation to S_1, as found in earlier work (29, 31), the wave packet has additional kinetic energy, and thus, much bigger portions are able to reach the nonreactive CoIn seam and relax to S_0 without breaking the planar symmetry.

The photoisomerization kinetics is shown in Fig. 7, *Top*. Once the wave packet reaches the reactive CoIn around 160 fs, the S_1 population starts to decrease, and S_0 is continuously populated. After 200 fs, parts of the wave packet start to be absorbed in the *cis*-S_0 minimum, counting to the product yield. After 900 fs, the product yield amounts to 44%, with 13% population still remaining in S_1 and 7% in S_0, and 36% have exited the numerical grid in the symmetric bending direction and are not considered in our simulations any further.

We probe the coherence at the CoIn by simulating the TRUE-CARS signal (transient redistribution of ultrafast electronic coherence in attosecond Raman signals). While we do not discuss it in detail, suffice it to say that it can extract experimentally the

vibronic coherence structure around the CoIn (52, 53). The signal reads (54)

$$S(\omega, T) = 2\,\mathrm{Im} \int_{-\infty}^{\infty} dt\, e^{i\omega(t-T)} \varepsilon_0^*(\omega)\varepsilon_1(t-T) \quad [8]$$
$$\times \langle \Psi_a(t)|\hat{\alpha}_{ab}|\Psi_b(t)\rangle,$$

where $|\Psi_{a/b}\rangle$ are the total nuclear-electronic states in the adiabatic representation; $\hat{\alpha}_{ab}$ is their transition polarizability; and ε_0 and ε_1 are the broadband (500 as) and narrowband (3 fs) X-ray pulses, respectively. These induce an off-resonant stimulated Raman process between two electronic states, and the signal is given by the time-integrated rate of change of photon numbers in the ε_0 field. TRUECARS is a sensitive probe of CoIns as it only exists if there is an electronic coherence.

The TRUECARS signal in Fig. 7 is nonvanishing right from the beginning at 20 fs as tails of the wave packet have already reached the nonreactive CoIn. It gets stronger during the dynamics when the reactive CoIn is reached by other parts of the wave packet and persists throughout the propagation time the wave packet passes through the CoIn. As demonstrated before (52), the vibronic coherence evolves with a dynamical phase according to the energy difference of the adiabatic states. This information is encoded in the positive gain (red)/negative loss (blue) oscillations at a given Raman shift. For a clear visualization, we took the signal trace $S(t)$ at $\omega_r = 0.3$ eV and calculated the frequency-resolved optical gating (FROG) (55) spectrogram

$$I_{\mathrm{FROG}}(\omega_c, \tau) = \left| \int_{-\infty}^{\infty} S(t) E_{gate}(t-\tau) e^{-i\omega_c t}\, dt \right|^2. \quad [9]$$
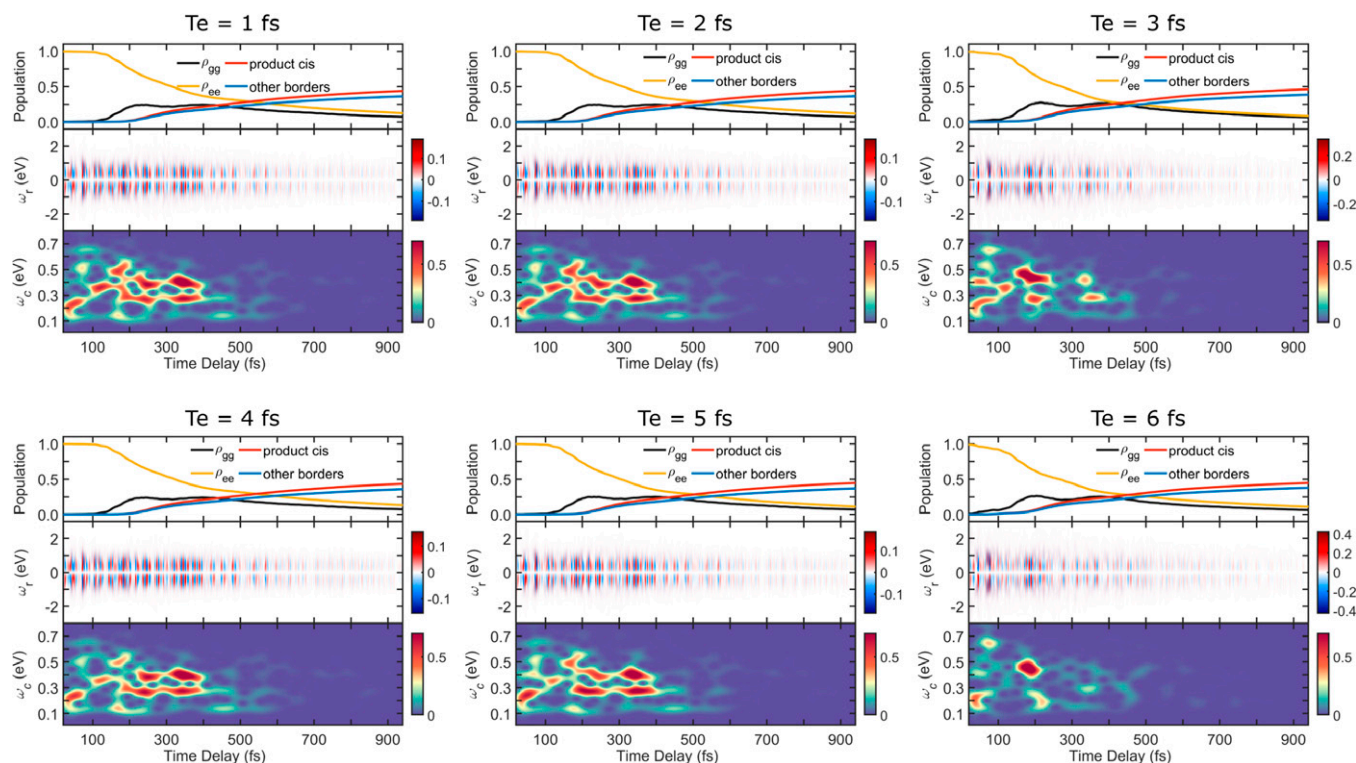
Fig. 8. Photoisomerization dynamics following two-photon excitation with quantum light (entangled photons). Panels correspond to Fig. 4 where the starting wave packets are displayed. For each set of three panels, *Top* shows population dynamics with the ground and exited state populations ρgg and ρee, the product yield as the cumulative amount of wave packet that has been absorbed in the cis minimum, and the cumulative amount of population that has been absorbed at the symmetric bending grid borders. *Middle* shows TRUECARS signal according to Eq. **8** being strong from the beginning, as parts of the nuclear wave packet immediately reach the CoIns and fading out with time. *Bottom* shows spectrogram of the TRUECARS signal according to Eq. **9** revealing the vibronic coherence distribution. In contrast to there, the photochemical yield is slightly affected by a few percent. The strongest difference is in the vibronic coherence distribution revealed by the TRUECARS spectrogram. This shows that the transition state of the photochemistry can be severely influenced by quantum light.

Gu et al.
Photoisomerization transition state manipulation by entangled
two-photon absorption

PNAS | 7 of 9
https://doi.org/10.1073/pnas.2116868118

This spectrogram, depicted below the TRUECARS signal in Fig. 7, reveals the time-dependent vibronic coherence structure stretching from 0.1 to 0.7 eV with major contributions around 0.2 to 0.4 eV.

We next turn to the isomerization kinetics. TRUECARS signals and FROG spectrograms for the six initial wave packets in Fig. 5 are shown in Fig. 7. The latter were created by classical TPA without entanglement. Neither the kinetics or product yield, nor the coherence structure associated with the CoIn is changing. We observe that modifying the bandwidth of the classical near-IR fields gives no control opportunity for the reaction path.

As shown in Fig. 4, photon entanglement has a stronger effect on the excited wave packets compared to their classical counterparts. Fig. 8 depicts the photoisomerization dynamics following ETPA with different entanglement times (Eq. 2). In contrast to their classical counterparts, the entanglement time does effect the isomerization yield, varying from 47% for T_e = 3 fs to 41% for T_e = 9 fs. Photon entanglement is thus able to add a control knob for photochemistry not available by classical light sources.

The strongest photon entanglement effect manifests the TRUECARS spectrogram and thus reveals the vibronic level structure of the CoIn. This is illustrated in Fig. 8, where the spectrograms for T_e = 3 fs and T_e = 6 fs are significantly different from the other ones. The vibronic coherence around the CoIn, and thus the transition state of the isomerization, is thus strongly modulated.

Conclusions

Entangled light provides a coherent control scheme for nuclear wave packets in a one-photon dark excited state of molecules. This is demonstrated by nonadiabatic CoIn wave packet dynamics for the *trans–cis* photoisomeriza-tion of azobenzene. This control leads to a substantial difference in the transient coherences during the passage through a CoIn, i.e., the transition state structure of the photochemistry, which we detect by a stimulated X-ray Raman signal. Additionally, the photoisomerization yield is noticeably affected by modulating the photon entanglement time. The essential role of energy–time entanglement in the control is clearly demonstrated by contrasting the quantum light–excited wave packets to that created by classical light. Varying the bandwidth alone for both classical nonchirped and chirped pulses leads to minor differences in the two-photon excitation process. Our results provide a strategy for coherent quantum light control of the photoexcitation of electronic dark states of molecules. This can have important applications in photoswitches and biological sciences (35, 56) that require a low photon flux to prevent photodamage of fragile samples. Further prospects may include introducing additional control quantum light pulse during the course of the reaction (57).

Data Availability. All study data are included in the article and/or *SI Appendix*.

1. S. Mukamel et al., Roadmap on quantum light spectroscopy. *J. Phys. At. Mol. Opt. Phys.* **53**, 072002 (2020).
2. S. Mukamel, *Principles of Nonlinear Optical Spectroscopy* (Oxford University Press, 1995).
3. K. E. Dorfman, F. Schlawin, S. Mukamel, Nonlinear optical signals and spectroscopy with quantum light. *Rev. Mod. Phys.* **88**, 045008 (2016).
4. F. Li, T. Li, M. O. Scully, G. S. Agarwal, Quantum advantage with seeded squeezed light for absorption measurement. *Phys. Rev. Appl.* **15**, 044030 (2021).
5. F. Chen, S. Mukamel, Vibrational hyper-Raman molecular spectroscopy with entangled photons. *ACS Photonics* **8**, 2722–2727 (2021).
6. C. K. Hong, Z. Y. Ou, L. Mandel, Measurement of subpicosecond time intervals between two photons by interference. *Phys. Rev. Lett.* **59**, 2044–2046 (1987).
7. A. Eshun et al., Investigations of molecular optical properties using quantum light and Hong-Ou-Mandel interferometry. *J. Am. Chem. Soc.* **143**, 9070–9081 (2021).
8. D. A. Kalashnikov et al., Quantum interference in the presence of a resonant medium. *Sci. Rep.* **7**, 11444 (2017).
9. M. G. Raymer, A. H. Marcus, J. R. Widom, D. L. P. Vitullo, Entangled photon-pair two-dimensional fluorescence spectroscopy (EPP-2DFS). *J. Phys. Chem. B* **117**, 15559–15575 (2013).
10. T. Landes et al., Quantifying the enhancement of two-photon absorption due to spectral-temporal entanglement. *Opt. Express* **29**, 20022–20033 (2021).
11. H. Oka, Entangled two-photon absorption spectroscopy for optically forbidden transition detection. *J. Chem. Phys.* **152**, 044106 (2020).
12. F. Terenziani, C. Katan, E. Badaeva, S. Tretiak, M. Blanchard-Desce, Enhanced two-photon absorption of organic chromophores: Theoretical and experimental assessments. *Adv. Mater.* **20**, 4641–4678 (2008).
13. B. R. Mollow, Two-photon absorption and field correlation functions. *Phys. Rev.* **175**, 1555–1563 (1968).
14. F. Schlawin, K. E. Dorfman, S. Mukamel, Entangled two-photon absorption spectroscopy. *Acc. Chem. Res.* **51**, 2207–2214 (2018).
15. T. Li, F. Li, C. Altuzarra, A. Classen, G. S. Agarwal, Squeezed light induced two-photon absorption fluorescence of fluorescein biomarkers. *Appl. Phys. Lett.* **116**, 254001 (2020).
16. A. Eshun, Z. Cai, M. Awies, L. Yu, T. Goodson III, Investigations of thienoacene molecules for classical and entangled two-photon absorption. *J. Phys. Chem. A* **122**, 8167–8182 (2018).
17. K. M. Parzuchowski et al., Setting bounds on two-photon absorption cross-sections in common fluorophores with entangled photon pair excitation. *Phys. Rev. Applied* **15**, 044012 (2021).
18. H. Oka, Highly-efficient entangled two-photon absorption with the assistance of plasmon nanoantenna. *J. Phys. At. Mol. Opt. Phys.* **48**, 115503 (2015).
19. B. Gu, S. Mukamel, Manipulating two-photon-absorption of cavity polaritons by entangled light. *J. Phys. Chem. Lett.* **11**, 8177–8182 (2020).
20. T. Kang, Y. M. Bahk, D. S. Kim, Terahertz quantum plasmonics at nanoscales and angstrom scales. *Nanophotonics* **9**, 435–451 (2020).
21. J. Gea-Banacloche, Two-photon absorption of nonclassical light. *Phys. Rev. Lett.* **62**, 1603–1606 (1989).
22. A. R. Guzman, M. R. Harpham, O. Süzer, M. M. Haley, T. G. Goodson III, Spatial control of entangled two-photon absorption with organic chromophores. *J. Am. Chem. Soc.* **132**, 7840–7841 (2010).
23. O. Varnavski, T. Goodson III, Two-photon fluorescence microscopy at extremely low excitation intensity: The power of quantum correlations. *J. Am. Chem. Soc.* **142**, 12966–12975 (2020).
24. S. Szoke, M. He, B. P. Hickam, S. K. Cushing, Designing high-power, octave spanning entangled photon sources for quantum spectroscopy. *J. Chem. Phys.* **154**, 244201 (2021).
25. K. Hüll, J. Morstein, D. Trauner, In vivo photopharmacology. *Chem. Rev.* **118**, 10710–10747 (2018).
26. A. Goulet-Hanssens, F. Eisenreich, S. Hecht, Enlightening materials with photoswitches. *Adv. Mater.* **32**, e1905966 (2020).
27. T. Nägele, R. Hoche, W. Zinth, J. Wachtveitl, Femtosecond photoisomerization of cis-azobenzene. *Chem. Phys. Lett.* **272**, 489–495 (1997).
28. T. Schultz et al., Mechanism and dynamics of azobenzene photoisomerization. *J. Am. Chem. Soc.* **125**, 8098–8099 (2003).
29. A. Nenov et al., UV-light-induced vibrational coherences: The key to understand Kasha rule violation in trans-azobenzene. *J. Phys. Chem. Lett.* **9**, 1534–1541 (2018).
30. O. Bozovic, B. Jankovic, P. Hamm, Using azobenzene photocontrol to set proteins in motion. arXiv [Preprint] (2021). https://arxiv.org/abs/2106.06289 (Accessed 11 June 2021).
31. J. K. Yu, C. Bannwarth, R. Liang, E. G. Hohenstein, T. J. Martínez, Nonadiabatic dynamics simulation of the wavelength-dependent photochemistry of azobenzene excited to the nπ* and ππ* excited states. *J. Am. Chem. Soc.* **142**, 20680–20690 (2020).
32. F. Aleotti et al., Multidimensional potential energy surfaces resolved at the RASPT2 level for accurate photoinduced isomerization dynamics of azobenzene. *J. Chem. Theory Comput.* **15**, 6813–6823 (2019).
33. G. Bort, T. Gallavardin, D. Ogden, P. I. Dalko, From one-photon to two-photon probes: "Caged" compounds, actuators, and photoswitches. *Angew. Chem. Int. Ed. Engl.* **52**, 4526–4537 (2013).
34. G. Cabré et al., Rationally designed azobenzene photoswitches for efficient two-photon neuronal excitation. *Nat. Commun.* **10**, 907 (2019).
35. M. Dudek et al., Two-photon absorption and two-photon-induced isomerization of azobenzene compounds. *RSC Advances* **10**, 40489–40507 (2020).
36. H. Rau, E. Lueddecke, On the rotation-inversion controversy on photoisomerization of azobenzenes. Experimental proof of inversion. *J. Am. Chem. Soc.* **104**, 1616–1620 (1982).
37. E. Papagiakoumou et al., Functional patterned multiphoton excitation deep inside scattering tissue. *Nat. Photonics* **7**, 274–278 (2013).
38. W. Denk, J. H. Strickler, W. W. Webb, Two-photon laser scanning fluorescence microscopy. *Science* **248**, 73–76 (1990).
39. J. Javanainen, P. L. Gould, Linear intensity dependence of a two-photon transition rate. *Phys. Rev. A* **41**, 5088–5091 (1990).
40. C. Couteau, Spontaneous parametric down-conversion. *Contemp. Phys.* **59**, 291–304 (2018).
41. M. H. Rubin, D. N. Klyshko, Y. H. Shih, A. V. Sergienko, Theory of two-photon entanglement in type-II optical parametric down-conversion. *Phys. Rev. A* **50**, 5122–5133 (1994).
42. A. Muthukrishnan, G. S. Agarwal, M. O. Scully, Inducing disallowed two-atom transitions with temporally entangled photons. *Phys. Rev. Lett.* **93**, 093002 (2004).
43. B. Gu, D. Keefer, S. Mukamel, Wavepacket control and simulation protocol for entangled two-photon-absorption of molecules. arXiv [Preprint] (2021). https://arxiv.org/abs/2109.05146 (Accessed 11 September 2021).
44. R. J. Glauber, "Optical coherence and photon statistics" in *Quantum Theory of Optical Coherence* (John Wiley & Sons, Ltd, 2006), pp. 23–182.
45. D. Keefer et al., Imaging conical intersection dynamics during azobenzene photoisomerization by ultrafast X-ray diffraction. *Proc. Natl. Acad. Sci. U.S.A.* **118**, e2022037118 (2021).
46. M. H. Rubin, Transverse correlation in optical spontaneous parametric down-conversion. *Phys. Rev. A* **54**, 5349–5360 (1996).
47. H. B. Fei, B. M. Jost, S. Popescu, B. E. A. Saleh, M. C. Teich, Entanglement-induced two-photon transparency. *Phys. Rev. Lett.* **78**, 1679–1682 (1997).
48. S. P. Walborn, C. H. Monken, S. Pádua, P. H. Souto Ribeiro, Spatial correlations in parametric down-conversion. *Phys. Rep.* **495**, 87–139 (2010).

49. S. Mancini, V. Giovannetti, D. Vitali, P. Tombesi, Entangling macroscopic oscillators exploiting radiation pressure. *Phys. Rev. Lett.* **88**, 120401 (2002).
50. S. Lerch, A. Stefanov, Observing the transition from quantum to classical energy correlations with photon pairs. *Commun. Phys.* **1**, 1–6 (2018).
51. S. Butterworth, On the theory of filter amplifiers. *Exp. Wirel. Wirel. Eng* **7**, 536–541 (1930).
52. D. Keefer, T. Schnappinger, R. de Vivie-Riedle, S. Mukamel, Visualizing conical intersection passages via vibronic coherence maps generated by stimulated ultrafast X-ray Raman signals. *Proc. Natl. Acad. Sci. U.S.A.* **117**, 24069–24075 (2020).
53. D. Keefer *et al.*, Monitoring molecular vibronic coherences in a bichromophoric molecule by ultrafast X-ray spectroscopy. *Chem. Sci. (Camb.)* **12**, 5286–5294 (2021).
54. M. Kowalewski, K. Bennett, K. E. Dorfman, S. Mukamel, Catching conical intersections in the act: Monitoring transient electronic coherences by attosecond stimulated X-ray Raman signals. *Phys. Rev. Lett.* **115**, 193003 (2015).
55. R. Trebino *et al.*, Measuring ultrashort laser pulses in the time-frequency domain using frequency-resolved optical gating. *Rev. Sci. Instrum.* **68**, 3277–3295 (1997).
56. E. C. Carroll *et al.*, Two-photon brightness of azobenzene photoswitches designed for glutamate receptor optogenetics. *Proc. Natl. Acad. Sci. U.S.A.* **112**, E776–E785 (2015).
57. J. Cao, J. Che, K. R. Wilson, Intrapulse dynamical effects in multiphoton processes: Theoretical analysis. *J. Phys. Chem. A* **102**, 4284–4290 (1998).

CHEMISTRY

Gu et al.
Photoisomerization transition state manipulation by entangled
two-photon absorption

PNAS | **9 of 9**
https://doi.org/10.1073/pnas.2116868118